MR. XING ZHANG (Orcid ID : 0000-0002-4955-0500)

Article type : Research Article

Ti^{4+} modified $MgZrNb_2O_8$ microwave dielectric ceramics with an ultra-high quality factor

Xing Zhang, Cheng Liu*, Liang Shi, Wenhao Xu, Hongyang Zhang, Rui Zeng, Huaiwu Zhang

School of Electronic Science and Engineering, University of Electronic Science and Technology of China, Chengdu, 610054, China

Abstract

Ti^{4+} modified $MgZrNb_2O_8$ ($MgZr_{1-x}Ti_xNb_2O_8$, x = 0, 0.1, 0.2, 0.3, 0.4) ceramics were synthesized using the traditional solid-state reaction method. Pure $MgZr_{1-x}Ti_xNb_2O_8$ was detected without any secondary phase via the X-ray diffraction patterns. According to the sintering behavior and the surface morphology results, the introduction of Ti^{4+} reduced the sintering temperature and promoted the grain growth. The correlations between the dielectric properties and the crystal structure were analyzed through the Rietveld refinement and Raman spectroscopy. The slight shifts of the Raman peaks, corresponding to different vibration modes, were induced by the substitution of Ti^{4+} for Zr^{4+} and related to the improved quality factor. In general, the sample of $MgZr_{0.9}Ti_{0.1}Nb_2O_8$ sintered at 1320 °C for 4 h exhibited promising microwave dielectric properties with an ultra-high $Q \times f$ value of 130,123 GHz (at 7.308GHz, 20 °C), which is potential for 5G communication applications.

Keywords: $MgZrNb_2O_8$, microwave dielectric ceramics, ultra-high quality factor

Corresponding author: Cheng Liu, c_liu@uestc.edu.cn

---

1. Introduction

Microwave dielectric ceramic material, as one of the indispensable solutions for manufacturing

resonators and filters, is usually applied for high-frequency circuits (300MHz~300 GHz) with the advent of the 5G era [1, 2]. With the further limited promotion of device miniaturization, integration, and higher operating frequency, microwave dielectric ceramics should possess the following characteristics: higher dielectric constant, lower dielectric loss, and near-zero temperature coefficients of the resonance frequency [3-5].

$MgZrNb_2O_8$ ceramic system, as one of the promising material candidates for resonators and microwave dielectric filters, was first synthesized by Ramarao et al. through the solid reaction method with excellent microwave dielectric properties obtained: ε_r = 16.7, $Q \times f$ = 58,500 GHz, τ_f = −49.8 ppm/°C [6]. Pan et al. reported that the $MgZrNb_2O_8$ ceramics with wolframite structure, prepared by a simple and effective reaction sintering method for the first time, exhibited promising microwave dielectric properties: ε_r = 26.54, $Q \times f$ = 57,477 GHz, and τ_f = −17.69 ppm/°C [7]. Xiao et al. found that the quality factor was notably increased to 74,534.4 GHz via Ni^{2+} substituting for Mg^{2+} [8]. In addition, Xiao et al. improved the microwave dielectric performance in $MgZrNb_2O_8$ ceramics with an appropriate amount of Ge^{4+}/Sn^{4+} substitution for Zr^{4+} [9, 10]. The studies on $AZrNb_2O_8$ (A = Mn, Mg, Zn, Co) ceramics uncovered that $MgZrNb_2O_8$ and $ZnZrNb_2O_8$ systems possessed similar crystal structures [6]. It was also reported that the crystal structure of $ZnZrNb_2O_8$ was tailored by TiO_2 modification along with a tunable τ_f value, which was adjusted to −2.4 ppm/°C in the sample of $0.3ZnZrNb_2O_8$-$0.7TiO_2$ [11]. Moreover, Xiang et al. discovered that the dielectric properties were significantly improved via Zr^{4+} substitution with Ti^{4+}: ε_r = 29.75, $Q \times f$ = 107,303 GHz, and τ_f = −24.41 ppm/°C [12]. Huang et al. reported a positive effect of Zr substitution on the microstructure and microwave dielectric properties of $Zn(Ti_{1-x}Zr_x)Nb_2O_8$ ceramics [13].

On the basis of previous reports, $MgZr_{1-x}Ti_xNb_2O_8$ (x = 0, 0.1, 0.2, 0.3, 0.4) ceramics were prepared and studied systematically, aiming at improving the microwave dielectric performance while illustrating the correlations between the dielectric properties and the crystal structure. The substitution of Zr^{4+} by Ti^{4+} effectively reduces the optimal sintering temperature and significantly

improves the $Q \times f$ value (the maximum $Q \times f$ value is 130,123 GHz for x = 0.1).

2. Experiment procedure

$MgZr_{1-x}Ti_xNb_2O_8$ (x = 0, 0.1, 0.2, 0.3, 0.4) ceramics were prepared via the traditional solid-state reaction route via using the analytical reagent oxide powders of MgO (98%), ZrO_2 (99%), TiO_2 (99%), and Nb_2O_5 (99.9%) as raw materials (Aladdin Industrial Co, Shanghai, China). The materials were weighed, mixed with deionized water, grounded in nylon containers with zirconia milling balls for 12 h. After drying and sieving, the mixtures were calcined at 1100 ℃ for 3 h and milled for another 12 h. Then the calcined powders were evenly mixed with polyvinyl alcohol (PVA) as a binder (13 wt.%) and pressed into cylinders with 6 mm in thickness and 12 mm in diameter. The white cylinders were sintered from 1240 ℃ to 1340 ℃ in air for 4h.

Archimedes method was adopted to measure the bulk density of the as-sintered ceramics. The theoretical density was calculated via Equation (1):

$$\rho_{theory} = \frac{ZA}{V_C N_A} \quad (1)$$

where Z, A, V_C, and N_A are the number of atoms in the unit cell, the atomic weight (g/mol), the volume of the unit cell (cm^3), and the Avogadro number(mol^{-1}), respectively [9]. The relative density was calculated by Equation (2):

$$\rho_{relative} = \frac{\rho_{bulk}}{\rho_{theory}} \times 100\% \quad (2)$$

The ceramic surface morphology was observed via a scanning electron microscope (SEM, JEOL JSM-6490, Tokyo, Japan). The phase structure was identified using an X-ray diffraction (XRD, Rigaku D/max 2550 PC, Tokyo, Japan), with a 2θ range of 20 °-80 ° and a scanning rate of 4 °/min. The crystal structure was obtained through refining the XRD data using the FullProf software. The bond valence was calculated according to the XRD refinement data. Raman spectroscopy was collected through an InVia Raman microscope (Renishaw, UK) with the frequency in 100-1000 cm^{-1} range. The microwave dielectric properties were obtained at 20 °C, in the frequency range of 6-9 GHz using a Vector Network Analyzer (N5230, Agilent Technologies,

USA). The temperature coefficient of resonant frequency (τ_f) was calculated by the following Equation:

$$\tau_f = \frac{f_2 - f_1}{(80-20) \times f_1} \times 10^6 \quad (3)$$

where f_1 and f_2 were the resonant frequency measured at 20 °C and 80 °C, respectively.

3. Results and discussion

3.1. Sintering behaviors

Figure 1 shows the relative density values of the $MgZr_{1-x}Ti_xNb_2O_8$ (x = 0, 0.1, 0.2, 0.3, 0.4) ceramics at different sintering temperatures between 1240 °C and 1340 °C. From Fig 1, it is observed that the relative density values for all samples increase first with the sintering temperature and reach maximum values for diverse compositions at their corresponding optimal sintering temperatures. The relative density values for all samples are above 95% at the sintering temperatures ≥ 1300 °C, indicating that dense crystallinity is obtained. It is noticed that the optimal sintering temperature for x = 0.1 is 1320 °C, where the maximum relative density is obtained. The densification process is mainly ascribed to the elimination of pores inside the grains with the increase of sintering temperature. However, further increase of the sintering temperature promotes the growth of the grain boundary and hinders the elimination of pores, which in turn, results in the decline of the relative density. It is also noticed that the optimal sintering temperature shifts towards lower temperature with increasing x, indicating that the substitution of Ti^{4+} for Zr^{4+}promotes the densification process. As known, TiO_2 is more active than ZrO_2, thus it is easier to reach a high- energy activation state in Ti modified ceramic systems [12]. The introduction of Ti^{4+} is beneficial for the densification of the $MgZr_{1-x}Ti_xNb_2O_8$ ceramics.

Figure 2(a-e) shows the SEM micrographs of the $MgZr_{1-x}Ti_xNb_2O_8$ (x = 0, 0.1, 0.2, 0.3, 0.4) ceramics at their corresponding optimum sintering temperatures. All samples are characterized by dense morphology with few pores observed. In general, the average grain size is determined by the linear intercept method and the grain shape is assumed to be a tetrakaidecahedron. Thus, the average grain size is estimated via Equation (4):

$$D = \alpha d \quad (4)$$

where α is the collection factor of 1.65 and d is the linear intercept derived from SEM results [14,15]. The variation of the average grain size is present in Fig 2(f), from which the value of average grain size varies from 3.390 ± 0.074 μm for x = 0.0 to 4.506 ± 0.153 μm for x = 0.1, then decreases monotonously to 2.67 ± 0.128 μm for x = 0.4, indicating that a small amount of Ti^{4+} substitution promotes the grain growth but further increasing the Ti-substitution level inhibits the grain development. In addition, rod-shaped grains are observed from Fig 2(e). Fig 2(g) and Fig 2(h) present the EDS results of the rod-shaped grain marked in yellow circle and normal-shaped grain marked in red square from Fig 2(e), respectively. The atomic ratios of Zr and Ti elements from the rob-shaped grain (Zr : Ti = 4.85 : 3.43≈1.41) are approximately equal to those of the normal-shaped grain (Zr : Ti = 5.02 : 3.45≈1.45), indicating that no secondary phases or abnormal stoichiometric ratios are formed. The origin of the rob-shaped grains is usually from the deviation of the main crystal phase or grain amalgamation caused by grain growth and grain boundary diffusion [16].

3.2. XRD and Raman results

Figure 3(a) exhibits the XRD results of the $MgZr_{1-x}Ti_xNb_2O_8$ (x = 0, 0.1, 0.2, 0.3, 0.4) ceramics sintered at 1320 °C for 4 h. All diffraction peaks are matched well with the record of $MgZrNb_2O_8$ (ICDD#48-0329). No secondary phases are detected within the scanning range. Fig 3(b) shows the enlarged diffraction peaks of (-1 1 1) and (1 1 1), which shift towards higher angles. As known, the ionic radius of Ti^{4+} (0.605 Å) is smaller than that of Zr^{4+} (0.72 Å). The introduction of Ti^{4+} for Zr^{4+} reduces the unit cell volume and twists the crystal structure [17, 18]. In order to further investigate the effect of Ti^{4+} substitutions on the crystalline structure, Rietveld refinements on the XRD data are performed via the FullProf software. The monoclinic wolframite structure of $ZnZrNb_2O_8$ with P2/c (NO.013) space group is adopted as the initial model [19].

Figure 4(a) shows the Rietveld refinement patterns of the $MgZr_{1-x}Ti_xNb_2O_8$ (x = 0.1) ceramic sintered at 1320 °C for 4 h. The corresponding crystal structure pattern of $MgZrNb_2O_8$ is present in Fig 4(b). The refinement parameters are listed in Table 1. The discrepancy factors of R_p and R_{wp}

are less than 15%, indicating that the refinement results are reliable [20]. The cell parameters (a, b, c) and the unit volume of the cell gradually decrease, which are consistent with the shift of the diffraction peaks, as shown in Fig 3(b). As the chemical bond theory is suggestive for further illumination of the microstructure, we listed the bond types and lengths obtained from the refinements in Table 2.

Figure 5(a) exhibits the Raman spectra of the $MgZr_{1-x}Ti_xNb_2O_8$ (x = 0, 0.1, 0.2, 0.3, 0.4) ceramics sintered at 1320 °C for 4 h. Deconvolved and fitted Raman spectra of the $MgZr_{1-x}Ti_xNb_2O_8$ (x = 0.1) ceramics are presented in Fig 5(b). Raman spectroscopy provides the information on microstructure, phase transition, and crystal defects via detecting the lattice vibration mode [21]. In general, the Raman scattering is influenced by the vibration symmetry and the variation of molecular polarizability. Based on the group theory and 30 vibration modes predicted, the optic and acoustic models of $MgZrNb_2O_8$ are defined as follows: $10A_g + 8B_g + 5A_u + 7B_u$, in which $10A_g + 5A_u$ are verified as the Raman modes and $8B_g + 7B_u$ are attributed to the Infrared modes [22]. From Fig 5(a), less than 30 vibration modes are observed as some vibration modes are overlapped near similar frequencies, and some vibration peaks are covered by the background. It is noticed that the Raman peaks in the region of 800-1000 cm^{-1} are high-intensity, indicating that the symmetric vibrations exist in this range. It is reported that the Raman peaks at 158 cm^{-1} and 413 cm^{-1} are induced by the Zr-O bonds stretching vibration [12]. The symmetric stretching vibrations of Nb-O bonds are appointed to 890 cm^{-1} and the peaks near 840 cm^{-1} are referred to asymmetric stretching vibrations of Nb-O bonds [23]. The slight deviation of these two peaks shift towards higher frequencies is observed with the increase of x, corresponding well with the diffraction peaks shift observed from Fig 3(b). We suggest that the introduction of Ti^{4+} reduces the volume of the unit cell (as Table 1 shows) and changes atomic distances in the ZrO_6 and NbO_6, which in turn, strengthens the bond covalence between the cation and Zr/NbO_6 [24, 25]. The Raman peaks at 366 cm^{-1} and 466 cm^{-1} originate from the O-Zr-O bending [22, 24].

3.3. Microwave dielectric properties

In general, the dielectric constant (ε_r) of the ceramics with single-phase is mainly related to the densification and the ionic polarizability [26, 27]. The ε_r values of the $MgZr_{1-x}Ti_xNb_2O_8$ (x = 0, 0.1, 0.2, 0.3, 0.4) ceramics with different sintering temperatures are shown in Fig 6(a). It is observed that the ε_r values for all samples except x = 0 increase at first, then decrease slightly with the sintering temperature rising, which is in accordance with the variation trend of the relative density, as shown in Fig. 1. As Shannon proposed, the ceramic dielectric polarizability (a_D) can be calculated by adding the combined ionic polarizability [28]. Therefore, the dielectric polarizability values of the $MgZr_{1-x}Ti_xNb_2O_8$ ceramics are obtained by Equation (5):

$$\alpha_D(MgZr_{1-x}Ti_xNb_2O_8)=\alpha_D(Mg^{2+})+(1-x)\alpha_D(Zr^{4+})+x\alpha_D(Ti^{4+})+2\alpha_D(Nb^{5+})+8\alpha_D(O^{2-}) \quad (5)$$

And the Clausius–Mosotti equation is adopted to calculate the theoretical dielectric constant(ε_{rtheo}) via the following Equation:

$$\varepsilon_{rtheo}=\frac{3V_m+8\pi\alpha_D}{3V_m-4\pi\alpha_D} \quad (6)$$

where V_m is the molar volume obtained from the Rietveld refinements [29]. It is concluded from Equation (6) that the ε_{rtheo} value is associated with the values of α_D and V_m. The value of α_D/V_m was calculated from further discussion about the dielectric constant. The values of ε_r, ε_{rtheo}, and α_D/V_m for the $MgZr_{1-x}Ti_xNb_2O_8$ (x = 0, 0.1, 0.2, 0.3, 0.4) ceramics sintered at 1320 °C are exhibited in Fig 6(b). It is observed that the ε_r, ε_{rtheo}, and α_D/V_m values possess similar variation trends with x, indicating that the dielectric constants are mainly determined by the ion polarizability and the molar volume. Compared with the ionic polarizability, the molar volume decreases faster with the increase of x, which contributes to the increase of α_D/V_m value. In addition, the presence of “compressed” and “rattling” cations with low or high polarizabilities in the polyhedrons can be attributed to the introduction of Ti^{4+}, which contributes to the enhanced ε_r values higher than that of the ε_{rtheo} [28].

Figure 7(a) exhibits the quality factors ($Q \times f$) values of the $MgZr_{1-x}Ti_xNb_2O_8$ (x = 0, 0.1, 0.2, 0.3, 0.4) ceramics sintered at different temperatures. For the samples of x > 0, the $Q \times f$ values increase first with the sintering temperature and reach to maximum, then decrease. Especially, the

maximum $Q \times f$ value of 130,123 GHz is obtained at 1320 °C for the sample of x = 0.1. As known, the $Q \times f$ value is mainly depended on the internal factors (such as crystal structure) and external factors (such as the density, the second phase, grain size, and grain boundaries) [26, 30]. For the $MgZr_{1-x}Ti_xNb_2O_8$ ceramics with a single phase, the densification is the main impact that affects the $Q \times f$ value. Fig 7(b) shows the variation of the $Q \times f$ values and the Full Width at Half Maximum (FWHM) values at 840 cm^{-1} for the samples sintered at 1320 ^oC. The FWHM values are extracted through the fitting lines of the Raman spectra, which decrease first and then increase with x. The minimum value of the FWHM is obtained at x = 0.1. The $Q \times f$ value increases inversely with the damping behavior become weaker, and the FWHM of vibration mode is positively correlated with the damping behavior [31]. Thus, two opposite variation trends are observed for the $Q \times f$ and FWHM values. In addition, the optimal $Q \times f$ value showed in Fig 7(a) increases first and then decreases with x, which is in accordance with the grain size variation exhibited in Fig 2(f). As previously reported, the $Q \times f$ value can also be affected by the average grain size. According to Penn et al, the dielectric loss is optimal for small grain sizes of sintered alumina [15]. In this study, we find that the ceramics with large grains possess higher Q × f values, which behave similar with the BaMgTaO system [32]. As known, the dielectric loss is affected by intrinsic and extrinsic factors and not only related with the average grain size. Therefore, more efforts are still needed to clarify the specific relationship between the grain size and the dielectric loss.

It is well known that the grain boundaries, as two-dimensional defects, usually contribute to the increment of dielectric loss. The increase of the average grain size value induces the reduction of the two-dimensional defects, known as the grain boundary, which suppresses the dielectric loss [32]. Therefore, the $Q \times f$ value is closely related to the relative density, the FWHM, and the grain size effects.

The temperature coefficient of resonance frequency (τ_f) is influenced by the dielectric constant temperature coefficient (τ_ε) and the linear thermal expansion coefficient (α_L) [33, 34]. The τ_f can be

calculated as follows:

$$\tau_f = -\frac{1}{2}\tau_\varepsilon - \alpha_L \quad (7)$$

For most dielectric ceramics, the α_L value is about 10 ppm/°C. Therefore, the τ_ε value is the crucial factor contributing to the τ_f value. According to previous studies, the τ_ε value is affected by the B-site bond valence [12, 35], which can be obtained via Equations (8) and (9):

$$V_i = \sum_j v_{ij} \quad (8)$$

$$v_{ij} = \exp(\frac{R_{ij} - d_{ij}}{b}) \quad (9)$$

where R_{ij} is the bond valence parameter, d_{ij} is the length of the bond between atoms *i* and *j*, and *b* is the determined constant equal to 0.37 Å, respectively [12]. The length of the bond is gained from the Rietveld refinement results and the calculated bond valence is listed in Table 3.

Figure 8 shows the τ_f values and bond valence of the $MgZr_{1-x}Ti_xNb_2O_8$ (x = 0, 0.1, 0.2, 0.3, 0.4) ceramics sintered at 1320 °C. The variation trend of the τ_f value is similar to that of the bond valence. The largest negative τ_f value and the smallest bond valence are obtained at x = 0.1, indicating that the B-site bond valence is closely related to the τ_f value in the $MgZr_{1-x}Ti_xNb_2O_8$ system. However, the τ_f value of $MgZr_{1-x}Ti_xNb_2O_8$ ceramic is still too high for practical applications. Further efforts are still needed to adjust the τ_f value to near zero via ion substitution (such as Mn^{2+}) and introduction of secondary phases with positive τ_f values (such as Li_2TiO_3 and $CaTiO_3$) [19, 36, 37].

4. Conclusion

In this work, pure $MgZr_{1-x}Ti_xNb_2O_8$(x = 0, 0.1, 0.2, 0.3, 0.4) ceramics were synthesized via the traditional solid-phase reaction route. The substitution of Ti^{4+} for Zr^{4+} reduced the sintering temperature, improved the relative density, and decreased the dielectric loss. An appropriate amount of Ti^{4+} substituting for Zr^{4+} could significantly improve the $Q \times f$ value. The ε_r value exhibited a positive correlation with the α_D/V_m value, while the τ_f value was closely related to the bond valence. Typically, the sample of $MgZr_{0.9}Ti_{0.1}Nb_2O_8$ ceramic exhibited promising

microwave dielectric properties sintered at 1320 °C for 4 h: ε_r = 25.72, $Q \times f$ = 130,123 GHz (the measurement frequency is 7.308GHz, the dielectric loss is 5.62E-5, and the measurement temperature is 20 °C), τ_f = -46.60 ppm/°C, which was promising for 5G microwave communication applications.

Acknowledgements

This work was supported by Sichuan Science and Technology Program (No. 2020YFG0108), the Major Science and Technology Specific Projects of Sichuan Province (No. 2019ZDZX0026), the National Natural Science Foundation of China (Grant No. 51672036), the National Key Scientific Instrument and Equipment Development Project (No.51827802), and the Fundamental Research Funds for the Central Universities (Grant No. ZYGX2019J021).

Reference

[1]. Tien LC, Chou CC, Tsai DS. Microstructure of $Ba(Mg_{1/3}Ta_{2/3})O_3$-$BaSnO_3$ microwave dielectrics. *Ceram Int*. 2000; 26(1):57-62. https://doi.org/10.1016/S0272-8842(99)00019-X

[2]. Xia WS, Zhang LY, Wang Y, *et al.* Extrinsic effects on microwave dielectric properties of high-Q $MgZrTa_2O_8$ ceramics. *J Mater Sci Mater Electron*. 2016; 27(11):11325-11330. https://doi.org/10.1007/s10854-016-5256-0

[3]. Reane IM, Iddles D. Microwave dielectric ceramics for resonators and filters in mobile phone networks. *J Am Ceram Soc*. 2006; 89(7):2063-2072. https://doi.org/10.1111/j.1551-2916.2006.01025.X

[4]. Wang W, Liu C, Shi L, *et al.* Effects of Li_2O-B_2O_3-SiO_2-CaO-Al_2O_3 glass addition on the sintering behavior and microwave dielectric properties of Li3Mg2NbO6 ceramics. *Appl Phys A Mater Sci Process*. 2019; 125(9):1-8. https://doi.org/10.1007/s00339-019-2894-0

[5]. Xiang R, Su H, Li Y, Lu Q, Tang X. Effects of LBSCA glass addition on the sintering characteristic and microwave dielectric properties of $ZnTiNb_2O_8$ ceramics. *J Mater Sci Mater Electron*. 2020; 31(16):13460-13468. https://doi.org/10.1007/s10854-020-03899-2

[6]. Ramarao SD, Murthy VRK. Crystal structure refinement and microwave dielectric properties of new low dielectric loss $AZrNb_2O_8$ (A: Mn, Zn, Mg and Co) ceramics. *Scr Mater*. 2013; 69(3):274-277. https://doi.org/10.1016/j.scriptamat.2013.04.018

[7]. Pan HL, Xing CF, Bi JX, Jiang XS, Mao YX, Wu H. Sintering characteristics and microwave dielectric properties of low loss $MgZrNb_2O_8$ceramics achieved by reaction sintering process. *J Alloys Compd*. 2016; 687:274-279. https://doi.org/10.1016/j.jallcom.2016.06.029

[8]. Xiao M, Lou J, Wei Y, Sun H, Li L, Zhang P. Effect of Ni^{2+} substitution on crystal structure and microwave dielectric properties for $MgZrNb_2O_8$ ceramics. *J Mater Sci Mater Electron*. 2018; 29(2):985-992. https://doi.org/10.1007/s10854-017-7996-x

[9]. Xiao M, He S, Lou J, Zhang P. Influence of Ge^{4+} substitution for Zr^{4+} on the microwave dielectric properties of $Mg(Zr_{1-x}Ge_x)Nb_2O_8$ $(0 \leq x \leq 0.4)$ ceramics. *Ceram Int*. 2018; 44(17):21585-21590. https://doi.org/10.1016/j.ceramint.2018.08.229

[10]. Xiao M, Lou J, Wei Y, Zhang P. Crystal structure and microwave dielectric properties of $MgZr_{1-x}Sn_xNb_2O_8$ ceramics. *Ceram Int*. 2018; 44(1):885-889. https://doi.org/10.1016/j.ceramint.2017.10.016

[11]. Lyu XS, Li LX, Zhang S, *et al*. Crystal structure and microwave dielectric properties of novel $(1-x)ZnZrNb_2O_8$-$xTiO_2$ ceramics. *Mater Lett*. 2016; 171:129-132. https://doi.org/10.1016/j.matlet.2016.02.003

[12]. Xiang R, Su H, Zhang Q, Li Y, Tang X. Crystal structure and improved microwave dielectric properties of $ZnZr_{(1-x)}Ti_xNb_2O_8$ ceramics. *J Mater Sci Mater Electron*. 2020; 31(6):4769-4779. https://doi.org/10.1007/s10854-020-03034-1

[13]. Huang Y, Li Y, Wang Z, Xie Z, Shen Z, Hong Y. Effects of Zr substitution on microstructure and microwave dielectric properties of $Zn(Ti_{1-x}Zr_x)Nb_2O_8$ ceramics. *Appl Phys A Mater Sci Process*. 2019; 125(1):1-6. https://doi.org/10.1007/s00339-018-2335-5

[14] Crossland IG, Clay BD. Diffusion creep and its inhibition in a stainless steel. *Acta Metall*, 1977;25(8):929-937. https://doi.org/10.1016/0001-6160(77)90180-8

[15] Penn SJ, Alford NMN, Templeton A, *et al*. Effect of porosity and grain size on the microwave dielectric properties of sintered alumina. *J Am Ceram Soc*. 1997;80(7):1885-1888.

https://doi.org/10.1111/j.1151-2916.1997.tb03066.x

[16]. Wang G, Zhang D, Li J, *et al.* Structural dependence of microwave dielectric performance of wolframite structured $Mg_{1-x}Ca_xZrNb_2O_8$ ceramics: Crystal structure, microstructure evolution, Raman analysis and chemical bond theory. *J Eur Ceram Soc*. 2021;41(6):3445-3451. https://doi.org/10.1016/j.jeurceramsoc.2021.01.033

[17]. Shannon RD. Revised effective ionic radii in halides and chalcogenides. *Acta Crystallogr*. 1976; A32:751-767. https://doi.org/10.1107/s0567739476001551

[18]. Liu C, Shi L, Lai Y, *et al.* B-site modification of $(Ba_{0.6}Sr_{0.4})TiO_3$ ceramics with enhanced diffuse phase transition behavior. *Ceram Int*. 2018; 44(7):8109-8115. https://doi.org/10.1016/j.ceramint.2018.01.255

[19]. Lai Y, Hong C, Jin L, *et al.* Temperature stability and high-Qf of low temperature firing Mg_2SiO_4-Li_2TiO_3 microwave dielectric ceramics. *Ceram Int*. 2017; 43(18):16167-16173. https://doi.org/10.1016/j.ceramint.2017.08.192

[20]. Xiao M, Lou J, Wei Y, He S, Zhang P. Effect of Co^{2+} substitution on crystal structure and microwave dielectric properties of $MgZrNb_2O_8$ ceramics. *J Alloys Compd*. 2018; 747:783-787. https://doi.org/10.1016/j.jallcom.2018.03.105

[21]. Shi L, Liu C, Zhang H, *et al.* Crystal structure, Raman spectroscopy, metal compatibility and microwave dielectric properties of $Ce_2Zr_3(MoO_4)_9$ ceramics. *Mater Chem Phys*. 2020; 250(March):122954. https://doi.org/10.1016/j.matchemphys.2020.122954

[22]. Zhang J, Zuo R, Cheng Y. Relationship of the structural phase transition and microwave dielectric properties in $MgZrNb_2O_8$-TiO_2 ceramics. *Ceram Int*. 2016; 42(6):7681-7689. https://doi.org/10.1016/j.ceramint.2016.01.182

[23]. Bi JX, Xing CF, Zhang YH, Yang CH, Wu HT. Correlation of crystal structure and microwave dielectric properties of $Zn_{1-x}Ni_xZrNb_2O_8$ ($0 \leq x \leq 0.1$) ceramics. *J Alloys Compd*. 2017; 727:123-134. https://doi.org/10.1016/j.jallcom.2017.08.110

[24]. Zhang Y, Zhang Y, Xiang M. Crystal structure and microwave dielectric characteristics of Zr-substituted $CoTiNb_2O_8$ ceramics. *J Eur Ceram Soc*. 2016; 36(8):1945-1951. https://doi.org/10.1016/j.jeurceramsoc.2016.02.026

[25]. Ramarao SD, Kiran SR, Murthy VRK. Structural, lattice vibrational, optical and microwave dielectric studies on $Ca_{1-x}Sr_xMoO_4$ ceramics with scheelite structure. *Mater Res Bull*. 2014; 56:71-79. https://doi.org/10.1016/j.materresbull.2014.04.064

[26]. Tang B, Xiang Q, Fang Z, *et al.* Influence of Cr^{3+} substitution for Mg^{2+} on the crystal structure and microwave dielectric properties of $CaMg_{1-x}Cr_{2x/3}Si_2O_6$ ceramics. *Ceram Int*. 2019; 45(9):11484-11490. https://doi.org/10.1016/j.ceramint.2019.03.016

[27]. Zhang P, Sun K, Mao X, Xiao M, Zheng Z. Crystal structures and high microwave dielectric properties in Li^+/Ti^{4+} ions co-doped $Li_3Mg_2NbO_6$ ceramics. *Ceram Int*. 2020; 46(6):8097-8103. https://doi.org/10.1016/j.ceramint.2019.12.036

[28]. Shannon RD. Dielectric polarizabilities of ions in oxides and fluorides. *J Appl Phys*. 1993; 73(1):348-366. https://doi.org/10.1063/1.353856

[29]. Song XQ, Du K, Li J, *et al.* Low-fired fluoride microwave dielectric ceramics with low dielectric loss. *Ceram Int*. 2019; 45(1):279-286. https://doi.org/10.1016/j.ceramint.2018.09.164

[30]. Lai Y, Tang X, Huang X, *et al.* Phase composition, crystal structure and microwave dielectric properties of $Mg_{2-x}Cu_xSiO_4$ ceramics. *J Eur Ceram Soc*. 2018; 38(4):1508-1516. https://doi.org/10.1016/j.jeurceramsoc.2017.10.035

[31]. Liao Q, Li L. Structural dependence of microwave dielectric properties of ixiolite structured $ZnTiNb_2O_8$ materials: Crystal structure refinement and Raman spectra study. *Dalt Trans*. 2012; 41(23):6963-6969. https://doi.org/10.1039/c2dt12451c

[32]. Ichinose N. Effect of grain size and secondary phase on microwave dielectric properties of $Ba(Mg_{1/3}Ta_{2/3})O_3$ and $Ba([Mg, Zn]_{1/3}Ta_{2/3})O_3$ systems. *J Eur Ceram Soc*. 2006; 26(10-11):1755-1759. https://doi.org/10.1016/j.jeurceramsoc.2005.09.032

[33]. Lee C Te, Ou CC, Lin YC, Huang CY, Su CY. Structure and microwave dielectric property relations in $(Ba_{1-x}Sr_x)_5Nb_4O_{15}$ system. *J Eur Ceram Soc*. 2007; 27(5):2273-2280. https://doi.org/10.1016/j.jeurceramsoc.2006.07.022

[34]. Wang G, Zhang D, Xu F, *et al.* Correlation between crystal structure and modified microwave dielectric characteristics of Cu^{2+} substituted $Li_3Mg_2NbO_6$ ceramics. *Ceram Int*. 2019; 45(8):10170-10175. https://doi.org/10.1016/j.ceramint.2019.02.066

[35]. Zhong M, Tang X, Li Y, Jing Y, Su H. Microwave dielectric properties, microstructure, and bond energy of $Zn_{3-x}Co_xB_2O_6$ low temperature fired ceramics. Ceram *Int*. 2020; 46(11):18667-18674. https://doi.org/10.1016/j.ceramint.2020.04.180

[36] Bi J, Yang C, Wu H. Correlation of crystal structure and microwave dielectric characteristics of temperature stable $Zn_{1-x}Mn_xZrNb_2O_8$ ($0.02 \leq x \leq 0.1$) ceramics. *Ceram Int*. 2017;43(1):92-98. https://doi.org/10.1016/j.ceramint.2016.09.115

[37] Huang CL, Weng MH. Improved high Q value of $MgTiO_3$-$CaTiO_3$ microwave dielectric ceramics at low sintering temperature. *Mater Res Bull*. 2001;36(15):2741-2750. https://doi.org/10.1016/S0025-5408(01)00752-8

Figure captions

Fig 1. Relative density values of the $MgZr_{1-x}Ti_xNb_2O_8$ (x = 0, 0.1, 0.2, 0.3, 0.4) ceramics sintered at different temperatures.

Fig 2. SEM images of the $MgZr_{1-x}Ti_xNb_2O_8$ (x = 0, 0.1, 0.2, 0.3, 0.4) ceramics sintered at their optimal sintering temperatures (a) x = 0.0, 1340 °C; (b) x = 0.1, 1320 °C; (c) x = 0.2, 1300 °C; (d) x = 0.3, 1280 °C; (e) x = 0.4, 1260 °C; the variation of the average grain size (f); and EDS analysis for the sample of x = 0.4 (g-h).

Fig 3. XRD patterns of the $MgZr_{1-x}Ti_xNb_2O_8$ (x = 0, 0.1, 0.2, 0.3, 0.4) ceramics sintered at 1320 °C for 4 h (a); and the enlarged (-1 1 1) and (1 1 1) diffraction peaks (b).

Fig 4. Rietveld refinement of the $MgZr_{1-x}Ti_xNb_2O_8$ (x = 0.1) ceramic sintered at 1320 °C for 4 h (a); and the crystal structure pattern of $MgZrNb_2O_8$ (b).

Fig 5. Raman spectra of the $MgZr_{1-x}Ti_xNb_2O_8$ (x = 0, 0.1, 0.2, 0.3, 0.4) ceramics sintered at 1320 °C for 4 h (a); and deconvolved and fitted Raman spectra of the $MgZr_{1-x}Ti_xNb_2O_8$ (x = 0.1) ceramics (b).

Fig 6. The ε_r values of the $MgZr_{1-x}Ti_xNb_2O_8$ (x = 0, 0.1, 0.2, 0.3, 0.4) ceramics with different sintering temperatures (a); and the ε_r, ε_{rtheo}, and α_D/V_m values for the $MgZr_{1-x}Ti_xNb_2O_8$ (x = 0, 0.1, 0.2, 0.3, 0.4) ceramics sintered at 1320 °C for 4 h (b).

Fig 7. Quality factors ($Q \times f$) values of the $MgZr_{1-x}Ti_xNb_2O_8$ (x = 0, 0.1, 0.2, 0.3, 0.4) ceramics with different sintering temperatures (a); and $Q \times f$, Raman FWHM values at 840 cm^{-1} of the $MgZr_{1-x}Ti_xNb_2O_8$ (x = 0, 0.1, 0.2, 0.3, 0.4) ceramics sintered at 1320 °C for 4 h (b).

Fig 8. Temperature coefficients of resonance frequency (τ_f) and bond valence of the $MgZr_{1-x}Ti_xNb_2O_8$ (x = 0, 0.1, 0.2, 0.3, 0.4) ceramics sintered at 1320 °C for 4 h.

Table captions

Table 1. Rietveld refinement results of the $MgZr_{1-x}Ti_xNb_2O_8$ (x = 0, 0.1, 0.2, 0.3, 0.4) ceramics sintered at 1320 °C for 4 h.

Table 2. Bond lengths(Å) obtained from the Rietveld refinements of the $MgZr_{1-x}Ti_xNb_2O_8$ (x = 0, 0.1, 0.2, 0.3, 0.4) ceramics sintered at 1320 °C for 4 h.

Table 3. Nb-site bond valence of the $MgZr_{1-x}Ti_xNb_2O_8$(x = 0, 0.1, 0.2, 0.3, 0.4) ceramics sintered at 1320 °C for 4 h.

Table 1

x	a(Å)	b(Å)	c(Å)	β	V_{cell}(Å^3)	R_p(%)	R_{wp}(%)
0	4.8031	5.6562	5.0875	91.407	138.1714	8.42	8.54
0.1	4.7889	5.6550	5.0810	91.338	137.5624	9.72	9.94
0.2	4.7755	5.6537	5.0752	91.239	136.9926	9.89	9.97
0.3	4.7621	5.6533	5.0694	91.103	136.4491	10.1	10.5
0.4	4.7467	5.6531	5.0630	90.930	135.7421	11.3	11.3

Table 2

Bond type	x=0	x=0.1	x=0.2	x=0.3	x=0.4
Mg/Zr-O(1) [1] × 2	2.06076	2.02383	2.04213	2.03488	2.07566
Mg/Zr-O(1) [2] × 2	2.20431	2.19848	2.19744	2.18401	2.15477
Mg/Zr-O(2) × 2	2.01466	2.01124	2.02931	2.02172	2.00173
Nb-O(1) × 2	1.89816	1.92461	1.90128	1.90776	1.88685
Nb-O(2)[1] × 2	1.99114	1.97914	1.96356	1.97033	1.92940
Nb-O(2)[2] × 2	2.17955	2.17718	2.16016	2.15545	2.20944

Table 3

x	Bond type	$R_{B\text{-site}}$	$v_{B\text{-site}}$	$V_{B\text{-site}}$	τ_f(ppm/°C)
0	Nb-O(1) × 2	1.911	1.0353 × 2	4.6490	-37.89
	Nb-O(2)^1 × 2		0.8052 × 2		
	Nb-O(2)^2 × 2		0.4839 × 2		
0.1	Nb-O(1) × 2	1.911	0.9638 × 2	4.5654	-46.60
	Nb-O(2)^1 × 2		0.8319 × 2		
	Nb-O(2)^2 × 2		0.4870 × 2		
0.2	Nb-O(1) × 2	1.911	1.0266 × 2	4.8083	-39.64
	Nb-O(2)^1 × 2		0.8675 × 2		
	Nb-O(2)^2 × 2		0.5099 × 2		
0.3	Nb-O(1) × 2	1.911	1.0087 × 2	4.7542	-42.15
	Nb-O(2)^1 × 2		0.8518 × 2		
	Nb-O(2)^2 × 2		0.5165 × 2		
0.4	Nb-O(1) × 2	1.911	1.0674 × 2	4.9306	-29.10
	Nb-O(2)^1 × 2		0.9514 × 2		

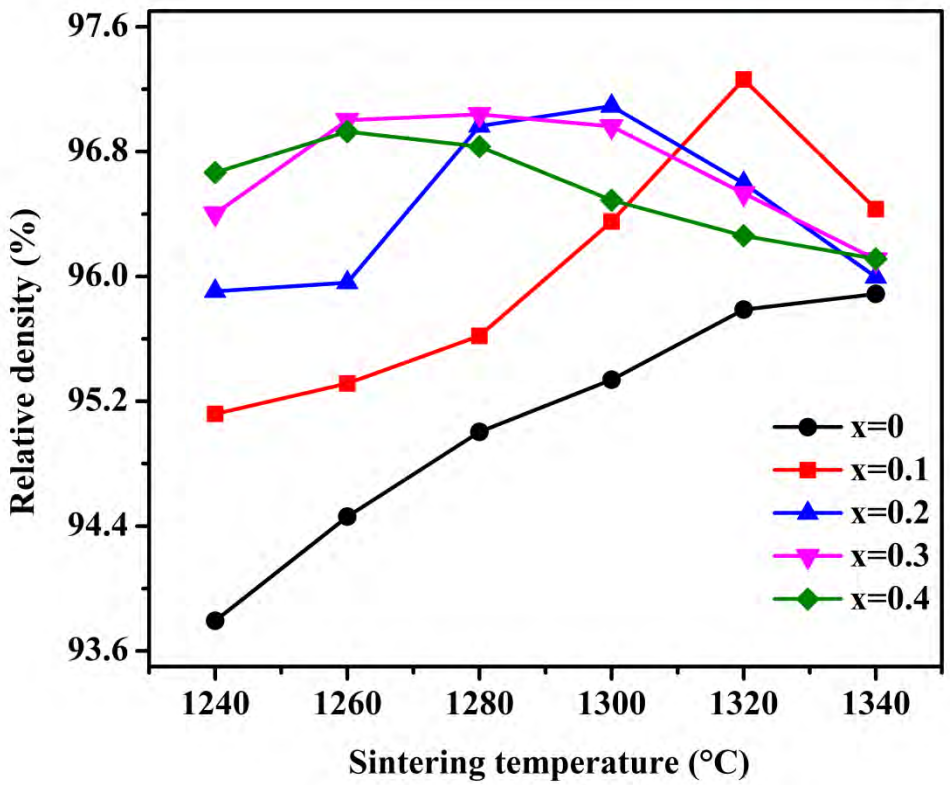

jace_17965_f1.tif

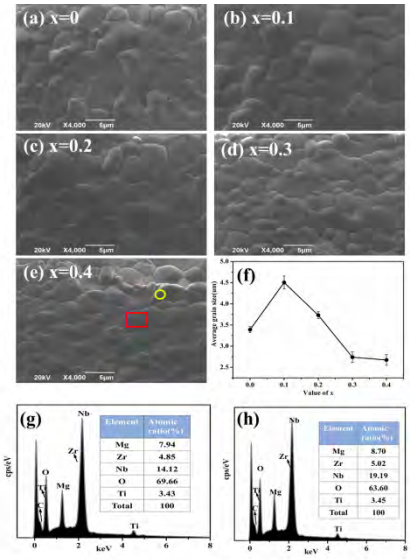

jace_17965_f2.tif

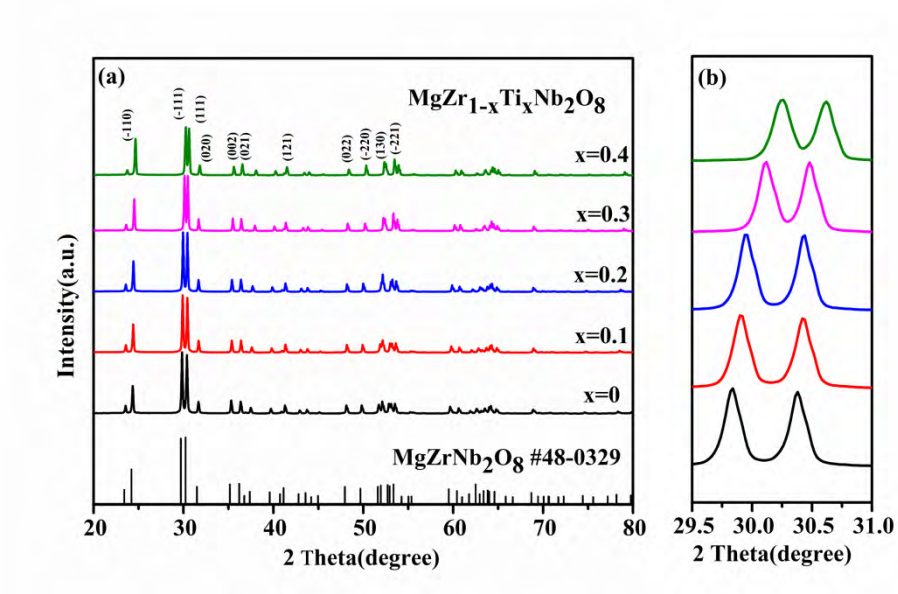

jace_17965_f3.tif

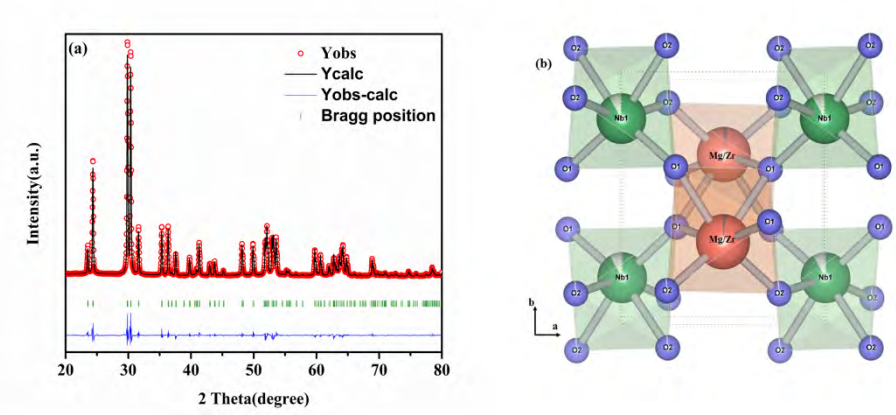

jace_17965_f4.tif

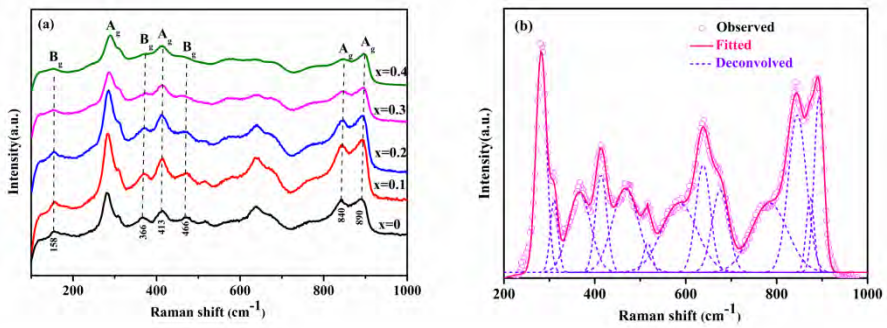

jace_17965_f5.tif

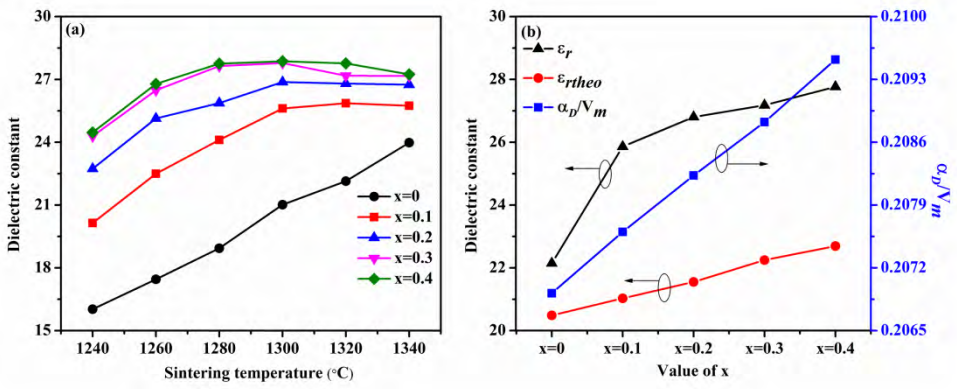

jace_17965_f6.tif

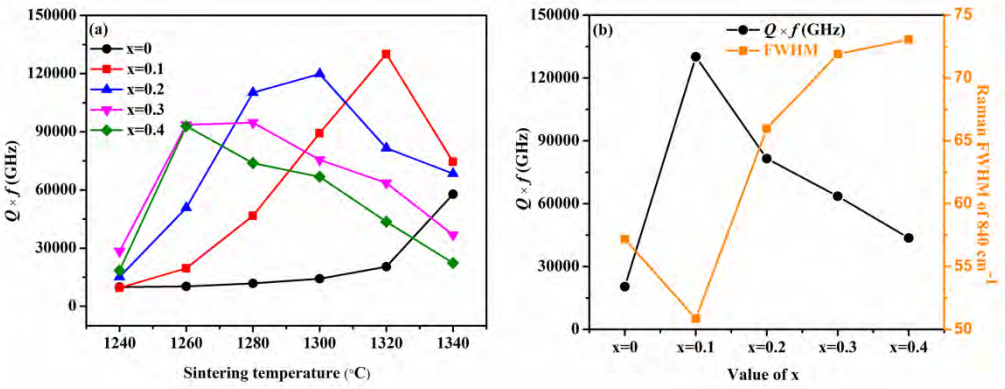

jace_17965_f7.tif

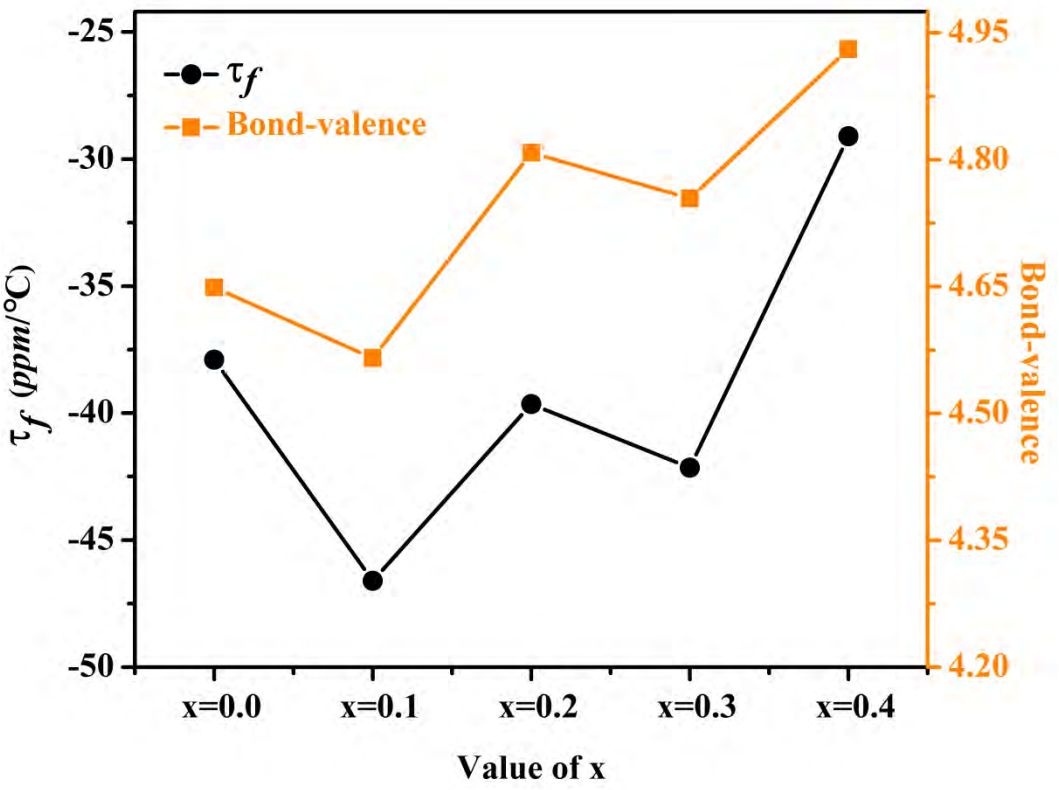

jace_17965_f8.tif